Composites Part C: Open Access 20 (2026) 100733

Contents lists available at ScienceDirect

Composites Part C: Open Access

journal homepage: www.sciencedirect.com/journal/composites-part-c-open-access

A recoverable composite auxetic absorber optimized for low-energy impacts

Sebastiano Di Mauro [a,*], Nejc Novak [b], Serena Graziosi [c], Raffaele Pugliese [d], Alessandro Galbiati [e], Alessandro Gadola [e], Alessandro Airoldi [a]

[a] *Department of Aerospace Science and Technology, Politecnico di Milano, Milan, Italy*
[b] *Faculty of Mechanical Engineering, University of Maribor, Maribor, Slovenia*
[c] *Department of Mechanical Engineering, Politecnico di Milano, Milan, Italy*
[d] *Nemo Lab, ASST Grande Ospedale Metropolitano Niguarda, Milan, Italy*
[e] *School of Industrial and Information Engineering, Politecnico di Milano, Milan, Italy*

ARTICLE INFO

Keywords:
Hexachiral auxetic structure
Recoverable absorbers
Energy absorption
Finite element modelling
Surrogate model
Optimization technique

ABSTRACT

This study proposes, validates, and optimizes an innovative recoverable composite energy absorber based on a foam-filled hexachiral auxetic architecture made of a visco-hyperelastic polymer. The absorber combined a 3D-printed hexachiral frame made of thermoplastic polyurethane reinforced by waste tire rubber (TPU-WTR) and a strain-rate-sensitive highly compressible open-cell polyurethane foam. While the combination of frame auxeticity with foam filling enhanced localized energy absorption, the specific materials adopted guaranteed full recoverability after impact and the variation of geometrical parameters in the hexachiral topology provided a significant design flexibility. A comprehensive mechanical characterization was performed, based on static and dynamic tests, which were used to calibrate accurately their numerical models. An absorber prototype was produced and experimentally tested, assessing the full recoverability at different impact velocities. Finite element models of the absorber were developed by using the identified material models and were validated from the quantitative and qualitative standpoint. Leveraging the design flexibility of the concept, fully parametric models were used to optimize a configuration for an impact of a 12 kg mass at 9 m/s, with a force constraint representative of the limit referred to a collision between a vehicle bumper and a pedestrian leg. The exploited Gaussian process regression (GPR) surrogate models, combined with a genetic algorithm, were able to predict the largely variable performance indices of the different configurations and enabled the identification of an optimal solution that significantly minimized the indentation of the impactor, while satisfying the force constraint and preserving full recoverability.

1. Introduction

In the last decades, the quest to develop lighter, stronger, and more efficient energy absorbers has been a driving force behind industrial and academic research, leading to innovative configurations with unique properties [1,2].

Many studies regarding energy absorbers consider a specific class of metamaterials, auxetic materials, which have the ability to exhibit negative Poisson’s ratio (NPR), becoming wider when stretched and thinner when compressed [3]. They have attracted significant interest thanks to their exceptional characteristics, including enhanced energy absorption capability, shear resistance, synclastic behavior, indentation resistance due to the prevention of material flow from the impacted area [4,5], and very promising innovative applications [6–8]. There are numerous studies focusing on auxetic energy absorbers under uniform compression and impact loads [9–11], while fewer studies examine the same type of structures under localized impacts [12–14], which deserve considerable interest. For example, in [15] a comparison between an auxetic-cored sandwich panel and a traditional aluminum foam-cored panel under a ballistic impact is described, whereas an innovative concept is proposed in [16,17], which is based on an auxetic hexachiral frame filled with foam to absorb indentation energy in an impact scenario. The latter two studies investigate the synergistic effect of an auxetic frame and a foam filler on the energy absorption performance.

---

[*] Corresponding author at: Department of Aerospace Science and Technology (DAER), Politecnico di Milano, Via La Masa, 34, 20156 Milano Italy.
E-mail address: sebastiano.dimauro@polimi.it (S. Di Mauro).

https://doi.org/10.1016/j.jcomc.2026.100733

Some studies have covered this topic of auxetic composites with fillings: in [18], the authors compare two specific auxetic composites with two non-auxetic composites subjected to a uniform compression, while the improvements given by the filler are highlighted in [19]; the mechanical properties of re-entrant honeycomb frames filled with polyurethane foam are investigated in [20,21]; the effects of foam filling on flexural properties of chiral cellular sandwich structures are analyzed in [22]; a recent literature review explored the classifications, mechanical responses, and underlying mechanisms of the auxetic composites with fillings [23]. Overall, as described in [8], auxetic composites with filling represent one of the top research hotspots of NPR materials in the last decades, and their use as energy absorption devices deserves attention and further investigation, also considering the capability to fabricate complex auxetic structures thanks to increasingly mature and commercially applicable additive manufacturing technologies [2,5,24,25].

Mechanical energy absorbers have been extensively employed in diverse contexts, including personal protection, crashworthiness in automotive and aerospace systems, as well as other engineering applications. A range of strategies has been investigated to design structures capable of dissipating mechanical energy efficiently, such as plastic deformation in ductile materials (metals and polymers), fragmentation in ceramics, and rate-dependent viscous processes [1,26–28]. Nevertheless, each one of these approaches is constrained by inherent limitations, in particular issues of recoverability and sensitivity to strain-rate effects. Recently, studies have focused on the fabrication of metamaterials with recoverable energy-absorbing behavior, suggesting novel strategies for mechanical energy dissipation [29]. One category is represented by ultralow-density hollow metallic and ceramic microlattices capable of fully recovering from large compressive strains while dissipating a considerable portion of the elastic strain energy through a buckling-related damping mechanism [30,31]. Another category includes structures with bistable elastic elements to be used as fully elastic and reusable energy-trapping structures [32–35]. While conventional elastic structures return to their original shape once the load is removed, structures with bistable elements snap between two distinct stable states and preserve their deformed configuration after unloading. Therefore, combining energy absorption with full recoverability enables the design of impact-protection devices with extended service life. Moreover, this recoverability enables the development of reusable structures that withstand repeated impacts while meeting crashworthiness requirements.

Accordingly, considerable progress has been made in the field of energy absorbers, and numerous innovative strategies with unique properties have been investigated. The category of NPR materials and the subcategory of foam-filled auxetic frames present particularly interesting aspects for the development of effective energy absorbers. However, there are few studies on feasible and practical engineering applications for this subcategory, despite all the promising improvements deriving by the synergistic interaction between the auxetic frame and the filling [23]. For these reasons, the aim of this study is the investigation of a specific auxetic composite with filling, namely a foam-filled hexachiral structure, with a recoverable behavior to be used in a low-energy impact scenario as a vehicle bumper. A fundamental novelty is represented by the material used for the hexachiral frame, which is fabricated using a viscoelastic material that allows complete recovery of the structure after impact, while ensuring the dissipation of kinetic energy. The use of a viscoelastic material in the auxetic frame introduces damping and impact-mitigation capabilities that offset the reduced stiffness typically associated with auxetic structures, improving their durability and stability under sustained deformation [36]. The paper also considers an engineering application, moving from some studies in the literature [37–44] on the design of vehicle bumpers based on metamaterials aimed at mitigating injuries to vulnerable road users (VRUs) such as pedestrians. However, to the best of the authors' knowledge, none has exploited a foam-filled hexachiral structure. Therefore, the design flexibility of the concept could be exploited to identify a configuration that optimized performance in a scenario representative of the aforementioned case study, by choosing specific values of impact velocity, geometry, and mass of the impactor. Accordingly, the concept of the foam filled recoverable viscoelastic auxetic absorbers is optimized to minimize the indentation required to maintain the force level below a limit related to the acceleration experienced by the impacted mass, by considering impact conditions and requirements chosen to be representative of a bumper impact on a pedestrian.

The manuscript is structured as follows: Section 2 describes the design and characterization of a recoverable foam-filled hexachiral structure, in particular, the experimental tests performed for the characterization of the materials used and the validation of finite element (FE) models of the foam-filled hexachiral structure through numerical-experimental correlations. Section 3 focuses on an engineering application of the foam-filled hexachiral structure in conditions representative of an automotive crash scenario, analyzed by exploiting an optimization procedure to find the best combination of geometrical parameters for designing the energy absorber and using the numerical technique of surrogate models. Finally, Section 4 summarizes the research findings.

2. Material characterization, design, and testing of a foam-filled hexachiral structure

2.1. Mechanism and design

The auxetic energy absorber investigated in this study was based on the hexachiral topology, one of the classes of chiral cellular structures, a distinct category of NPR materials. Such topology is notable for its pronounced auxetic behavior, which arises primarily from the rotation of cylindrical elements and the bending of ligaments. Fig. 1(a) shows the

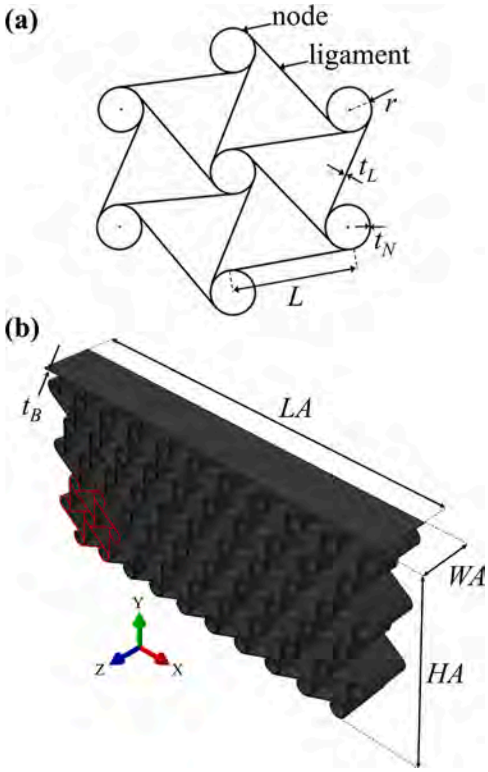

Fig. 1. Schematic drawings showing the main geometrical parameters: (a) fundamental hexachiral unit cell, (b) hexachiral structure with a unit cell highlighted in red (here a specific case with $Nx = 5$).

fundamental hexachiral unit cell, which consists of circular elements, acting as nodes, interconnected by six ligaments tangent to the nodes [9]. The ligament length L, the node radius r, and the thickness of the ligaments and nodes, t_L and t_N, respectively, represent the main geometrical parameters of the hexachiral unit cell, while the key parameter for the mechanical performance of the cellular structure is the L/r ratio.

Effective mechanisms of strength enhancement in this type of NPR material can be obtained thanks to the addition of a foam filling into the hollows of the hexachiral frame. These mechanisms can be described considering three main contributions: 1) the change in the deformation mode of both the auxetic frame and the filling, resulting in a more stable global deformation, which prevents or delays ligaments buckling and puts the filling in a state of biaxial compression; 2) the compression of the filling, which absorbs the impact energy thanks to its viscoelastic properties; 3) the friction between the frame and the filling and the constraints imposed by the filling on the deformation of the auxetic frame [23]. Furthermore, as demonstrated by several studies [6,10,18, 45], this type of chiral NPR structure, compared to another functional structure, namely the re-entrant honeycomb, exhibits isotropic in-plane behavior and preserves the auxetic effect over a larger deformation range, thanks to the rotational symmetry. These are desirable properties for an energy absorber, especially when loads are applied in different directions.

The hexachiral structure was parameterized considering the geometrical parameters reported in Table 1 and shown in Fig. 1. In this way, once the global dimensions of the hexachiral structure, i.e., *LA, WA,* and *HA*, are fixed, it is possible to build any hexachiral configuration within certain geometrical constraints. The boundary skin, at the top of the structure, was flat, though it could have any shape, enabling the design of a variety of geometric configurations. Lastly, it is worth noting that the number of fundamental unit cells in the vertical direction was a dependent parameter.

2.2. Mechanical properties of materials

2.2.1. Hexachiral frame material

Some research in the literature [36,46] justifies the use of thermoplastic polyurethane (TPU) filaments to fabricate, through 3D-printing technologies, energy absorbing auxetic structures, particularly in cases where structures must withstand both static and dynamic loads while maintaining their shape. For this reason, the 3D-printed auxetic hexachiral frame presented in this paper was made of TPU-WTR, a thermoplastic polyurethane with micronized waste tire rubber (80/20%wt) composite filament, hardness 80 Shore A, with a 1.75 mm diameter (Pneumatique, Treed Filaments, Italy). This peculiar elastomeric material was chosen for its interesting mechanical properties, which were superior to those of virgin TPU, and for the added value represented by the use of recycled materials. The main properties are as follows: density of 1150 kg/m^3, Poisson's ratio of 0.482, isotropic behavior (despite the different raster angles and printing temperatures), and viscoelastic behavior. Printability, mechanical behavior and morphological characteristics of this commercial filament were described in [47].

Table 1
Geometrical parameters of the hexachiral structure.

Geometrical parameter	Expression	Unit of measurement
Length of the structure	LA	mm
Width of the structure	WA	mm
Height of the structure	HA	mm
Number of fundamental hexachiral unit cells in horizontal direction	Nx	-
Characteristic ratio of the hexachiral unit cell	L/r	-
Thickness of the ligaments	t_L	mm
Thickness of the nodes	t_N	mm
Thickness of the boundary skin	t_B	mm

Due to the intrinsic variability of the recycled materials, a series of experimental tests were carried out for the present work to characterize the TPU-WTR both statically and dynamically. The tests carried out for the static response were uniaxial tensile, planar tensile, and uniaxial compression; these tests were useful for a direct calibration of the hyperelastic contribution. The dynamic response was analyzed by carrying out a series of indentation tests allowing the strain-rate sensitivity to be revealed and enabling inverse calibration of the viscoelastic contribution. The numerical calibration will be described later in Section 2.5.2.1.

The setup of all experiments is reported in Table 2, while some of the specimens are shown in Fig. 2 (a-d). All specimens were fabricated using the fused filament fabrication (FFF) technology by NemoLab research center using a Sharebot QXXL 3D printer with a nozzle diameter of 0.8 mm to prevent clogging by the WTR particles, 100% infill density, and a layer height of 0.4 mm. The other printing parameters adopted were in accordance with the optimization performed by Badini et al. in [47]. Thus, the printing temperature was set to 230°C, the raster angle to 0°, the plate temperature to 55°C, and the printing speed to 1000 mm/min. The extrusion width was set to 0.96 mm with an extrusion multiplier of 1.0, outline overlap of 75%, coasting distance of 2.5 mm, wipe distance of 5 mm, and retraction vertical lift of 1 mm.

All static tests were performed at a constant crosshead displacement of 50 mm/min and at room temperature. Force and displacement were recorded during each test, and the nominal (or engineering) stress and strain were calculated. The dynamic indentation tests were performed at room temperature, using the experimental setup shown in Fig. 2(e): a hemispherical stainless-steel impactor with a mass of 5.536 kg and a diameter of 16 mm impacted, perpendicularly, the cubic specimen, placed on a thick steel plate, at four different impact velocities. The drop weight was equipped with a 1 kN load cell to measure force over time. The testing machine was equipped with two photocells, allowing the measurement of the impact velocity of the indenter on the cubic specimen. The magnitude of the impact velocities was about 1.8, 2.7, 3.6, and 5.0 m/s.

The results of all experimental tests are reported in Fig. 3. Specifically, Fig. 3(a) shows the average nominal stress–strain curves of the static tests, while Fig. 3(b) highlights the different viscoelastic responses at different impact velocities in the dynamic indentation tests. The stress–strain curves of the uniaxial tensile and compression tests were consistent with the typical experimental results for elastomeric materials reported in the literature [48], whereas the stress–strain curve of the planar tensile test was considered acceptable up to a strain value of 15%. This was due to issues related to the clamping system that constrained the elastomeric specimens.

2.2.2. Filling material

The filling was CF45-M, one of the commercially available versions of Confor™ open-celled polyurethane (PU) foam, currently applied in the automotive and aerospace fields. Such open-cell foam has a density of 99 kg/m^3. The mechanical properties of the strain-rate sensitive PU

Table 2
Setup of the experiments carried out for the mechanical characterization of TPU-WTR.

Type of test	Testing machine	Specimen shape		Number of specimens
		Dimensions	Reference	
Uniaxial tensile	MTS Synergie 200	Type IV dogbone	ASTM D638-14	4
Planar tensile	MTS 858 Mini Bionix	140 × 2 × 105 mm^3	[49]	3
Uniaxial compression	MTS 858 Mini Bionix	12.7 × 12.7 × 25.4 mm^3	ASTM D695-23	3
Indentation	STEPLab Drop Weight	40 × 40 × 40 mm^3	-	4

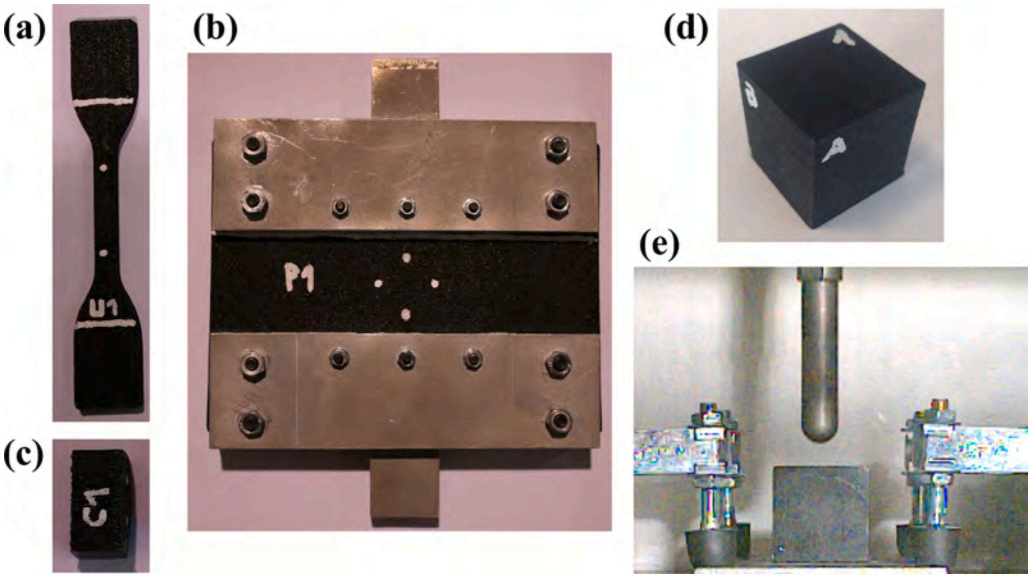

Fig. 2. Some of the specimens used for the mechanical characterization of TPU-WTR: (a) ASTM D638-14 type IV dogbone specimen U1 for uniaxial tensile test, (b) specimen P1 with a very high length to height ratio according to [49] for planar tensile test, (c) ASTM D695-23 specimen C1 for uniaxial compression test, (d) cubic sample D1 for indentation test, (e) front view of the experimental setup of the indentation test.

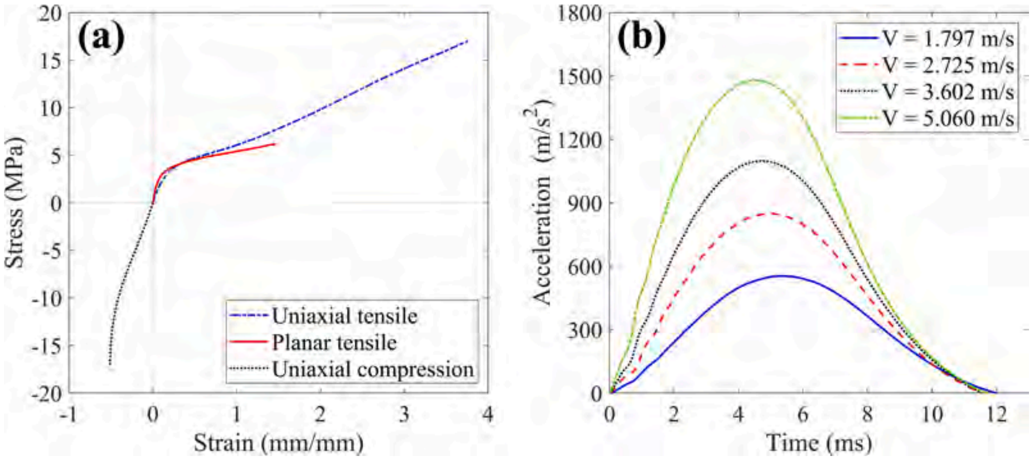

Fig. 3. Results of the experimental tests on TPU-WTR specimens: (a) average nominal stress–strain curves of the uniaxial tensile, planar tensile, and uniaxial compression tests, (b) average acceleration curves of the indentation tests for the four impact velocities.

foam adopted in this study were evaluated by testing nine foam specimens measuring approximately 50 × 50 × 25 mm^3, taking the

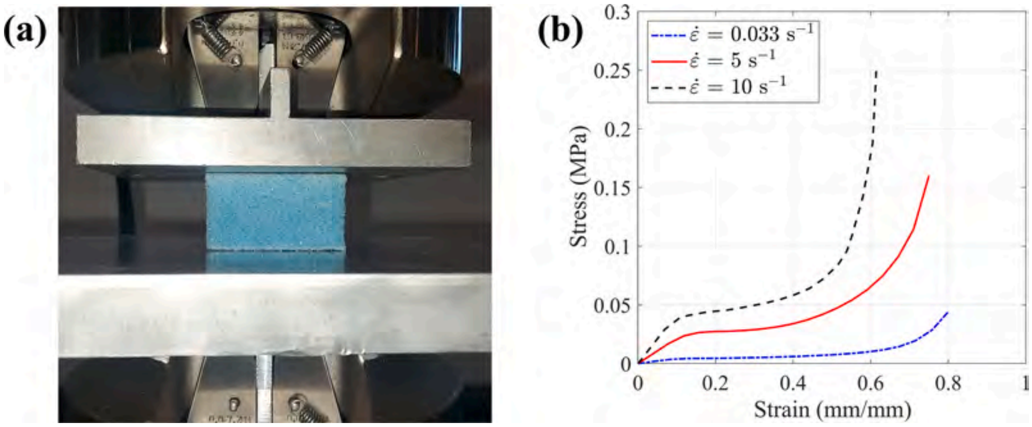

Fig. 4. Mechanical characterization of Confor™ PU foam through uniaxial compression test: (a) front view of the experimental setup, (b) average nominal stress–strain curves for the three strain rates.

ASTM D3574 Test C standard as a reference. Uniaxial compression tests were carried out using a MTS 858 Mini Bionix testing machine (Fig. 4(a)) at room temperature under three strain rates, specifically 0.033, 5 and 10 s^{-1}. The three average nominal stress–strain curves are shown in Fig. 4(b) and highlight the significant strain-rate sensitivity of the PU foam. The use of these curves is described later in Section 2.5.2.2.

2.3. Prototype manufacturing

A prototype representing a simple case of a foam-filled hexachiral structure was fabricated to investigate the energy absorber and validate the FE model. The hexachiral frame consisted of 2 cells in the X-axis (Nx) and 2 cells in the Y-axis, of which the top two were partially cut by the flat boundary skin, and could be considered as a parallelepiped with global dimensions 225 × 30 × 125 mm^3 ($LA \times WA \times HA$). The thicknesses of chiral ligaments (t_L), chiral nodes (t_N) and boundary skin (t_B) were 3.62, 3.66, and 3.06 mm, respectively. The characteristic L/r ratio was set equal to 4.0.

The 3D-printed hexachiral frame was fabricated with the FFF technology by NemoLab research center using a Sharebot QXXL 3D printer (Fig. 5(a)), adopting the same printing parameters used to fabricate the specimens for the mechanical characterization of the TPU-WTR (Section 2.2.1).

The foam inserts, both cylindrical and triangular prism-shaped, were cut from a sheet measuring 500 × 500 × 50 mm^3 using a band saw. The inserts had a width of 30 mm and characteristic cross-sectional dimensions of 20 mm for the diameter of the cylinders and 40 mm for the side of the equilateral triangles. Finally, the inserts were manually positioned in the hollows of the auxetic frame (Fig. 5(b)).

The average density of the foam-filled absorber resulted to be approximately 444 kg/m^3. The total mass was 287 g, of which 244 g was TPU-WTR and 43 g was CF-45 M. The foam volume fraction was about 67% of the structure's total volume.

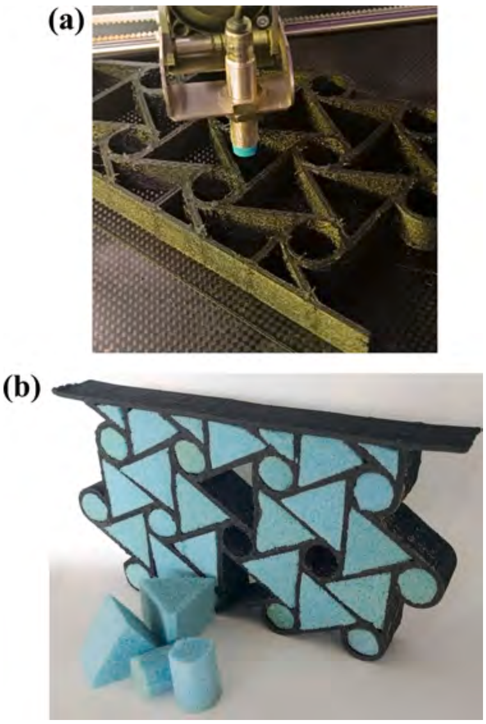

Fig. 5. Manufacturing of the hexachiral frame: (a) 3D-printing, (b) filling with Confor™ PU foam.

2.4. Drop-weight impact experimental setup

The energy absorber prototype was subjected to a series of six dynamic indentation tests, specifically drop-weight impacts. The experimental setup is shown in Fig. 6. A hemispherical stainless-steel impactor with a mass of 5.457 kg and a diameter of 100 mm impacted the prototype perpendicularly at two different impact velocities and at room temperature. Three tests were performed for each impact velocity in order to verify the repeatability of the test and, therefore, the recoverability of the energy absorber. Tests T1 to T3 were performed with an impact velocity V1 of 3.100 ± 0.025 m/s, whereas tests T4 to T6 were performed with an impact velocity V2 of 5.150 ± 0.037 m/s. After each impact, a few minutes were allowed for the viscoelastic absorber to recover completely. The energy absorber was placed on a thick stainless-steel plate and kept in position by four plexiglass guides to prevent lateral displacement during the collapse. The impactor was equipped with an accelerometer mounted on the top, which allowed the acquisition of vertical acceleration data at 20 kHz. The impact tests were recorded using a Phantom VEO E-310 L high-speed camera. The results of the tests are reported in Fig. 13 in the context of the numerical-experimental correlation.

2.5. FE model description

2.5.1. Generation of the hexachiral structure FE model

The FE model of the foam-filled hexachiral structure was generated using a Matlab® script similar to the one described in [17] and solved through the Simulia/Abaqus Explicit code [50]. The Matlab® script was based on the parameterization of the hexachiral frame and guided the generation of the model mesh and all the input files required for the Abaqus simulation. Geometrical parameters were those reported in Table 1. Both the cylindrical and triangular prism-shaped foam inserts were modelled using solid elements type C3D8 [50], while the auxetic frame was modelled using shell elements type S4 [50]. Generating a structure with the geometrical values reported in Section 2.3, resulted in a FE model consisting of 90,896 nodes and 74,754 elements, of which 14,460 were of type S4 and 60,294 of type C3D8. In Fig. 7(a) elements S4 are shown in black, while elements C3D8 are in cyan. The impactor, steel plate, and lateral guides were modelled as rigid analytical surfaces, as shown in Fig. 7(b).

The interactions in the model were simple contacts, modeled using the general contact algorithm available in the solver code [50]. A tangential contact interaction was set up between the two rigid surfaces, i.e., the impactor and the plate, and the auxetic frame, considering a friction coefficient of 0.9 [51]. No friction was set between the lateral guides and the whole structure. The impactor was free to move in the three directions, had a concentrated mass of 5.457 kg at its reference point, and the impact velocities V1 = 3.100 m/s and V2 = 5.150 m/s, set as initial velocities, were imposed downwards in the Y-direction.

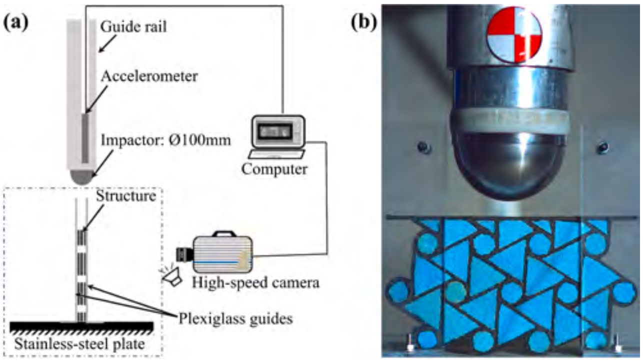

Fig. 6. Experimental setup: (a) schematic drawing (figure adapted from [17]), (b) front view of the experiment.

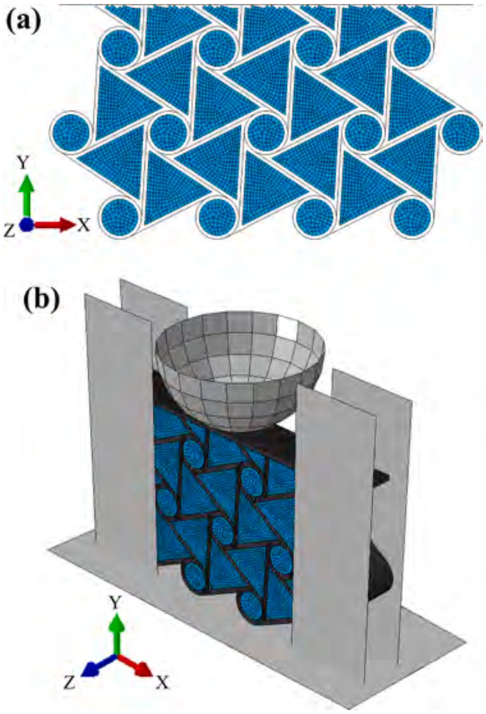

Fig. 7. FE model: (a) frontal view of the energy absorber only, (b) isometric view with the hemispherical impactor, the steel plate, the lateral guides and rendering of the shell thickness.

2.5.2. *Numerical model of the materials*

2.5.2.1. TPU-WTR. The TPU-WTR used for the hexachiral frame was represented as an isotropic visco-hyperelastic material, given its hyperelastic behavior, typical of elastomers, and its sensitivity to strain rate. The isotropic behavior of the 3D-printed filament was demonstrated in [47]. A modified generalized Maxwell model was then used to analytically describe the mechanical behavior of this visco-hyperelastic material [52–54].

In summary, the entire calibration was performed in two steps. First, the static experimental stress-strain curves were employed to directly calibrate the hyperelastic contribution by identifying the best-fitting form of strain energy potential. Second, once the hyperelastic contribution had been fixed, the inverse calibration of the viscoelastic contribution was performed similarly to the procedure presented in [54]. However, in the present study, a genetic algorithm on Matlab® was coupled with Abaqus FE simulations in an iterative procedure, with the aim of minimizing the differences between the experimental results of the indentation tests and the results of a FE model developed to replicate the experimental indentation tests.

The procedure is illustrated in a flowchart in Fig. 8 and is explained in detail below. The TPU-WTR was modelled by combining two material cards available in the Abaqus software. First, the hyperelastic contribution was modelled with the **HYPERELASTIC* material card [55], using the experimental curves of Fig. 3(a) for the direct calibration of the second order form of the Ogden strain energy potential. It is worth noting that the stress–strain curve of the planar tensile test was only used up to the acceptable point. This potential proved to be the most suitable form of strain energy potential, as demonstrated by numerical simulations on both uniaxial tensile and compression tests, as shown in Fig. 9 (a). Secondly, the viscoelastic contribution was modelled with the **VISCOELASTIC* material card [55], through a Prony series expansion whose coefficients were determined by taking as reference the ones used in [56]. This work was related to the numerical modelling of a TPU filament. The usage of this reference Prony series with eight terms returned a certain error, as shown in Fig. 9(b). For this reason, the Prony series used for the calibration was constituted by seventeen terms, adding new ones for smaller relaxation times comparable to the indentation event. So, the numerical-experimental correlation was optimized through a single-objective optimization procedure coupling the

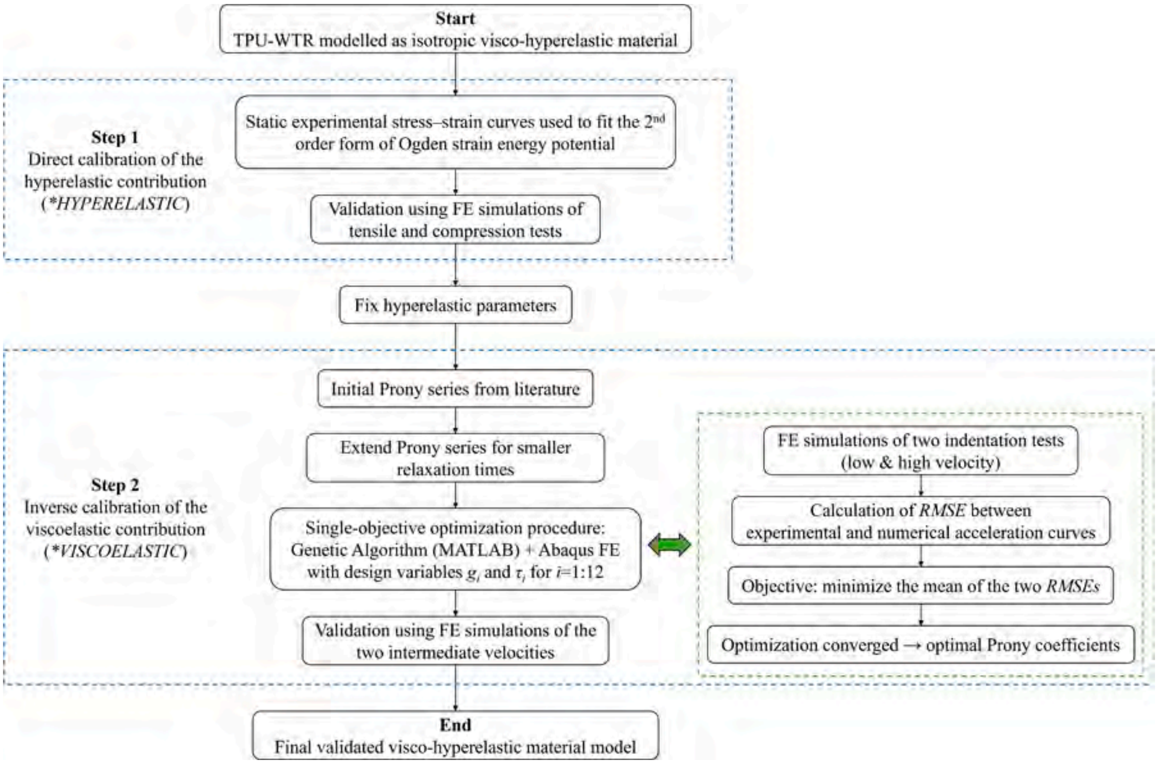

Fig. 8. Flowchart of the TPU-WTR calibration procedure.

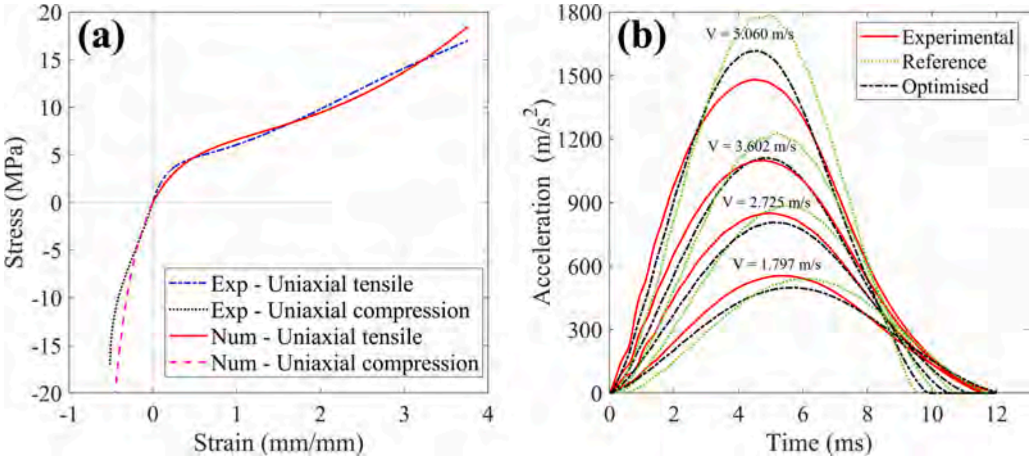

Fig. 9. Comparison of the experimental and numerical results on TPU-WTR: (a) nominal stress–strain curves of the uniaxial tensile and compression tests, (b) acceleration curves of the indentation tests for the four impact velocities with the dotted reference curves obtained using the Prony series from [56].

Matlab® function *ga* [57] and the FE simulations. The optimization considered the shear relaxation moduli, g_i, and the relaxation times, τ_i, of the first twelve terms of the Prony series as design variables, and kept the remaining terms fixed at the reference values. This choice was made after a sensitivity analysis on the coefficients. The response of the lowest impact velocity and the response of the highest impact velocity were used in the optimization procedure, and for each of them, the root mean square error (*RMSE*) between the experiment and the simulation was evaluated. The objective of the minimization was the average of these two *RMSEs*. The remaining two intermediate impact velocities were then used to validate the optimal results found. The results of the genetic optimization are shown in Fig. 9(b), where the experimental responses are compared with the numerical responses obtained with the optimized Prony series expansion. Therefore, the ability of the numerical model to reproduce the experimental response across different impact velocities demonstrated that the adopted formulation effectively captures the strain-rate dependent behavior of the TPU-WTR. This property is also highlighted by the numerical force-displacement curves of the impactor shown in Fig. 10, where it is evident that the mechanical response is dependent on the loading rate.

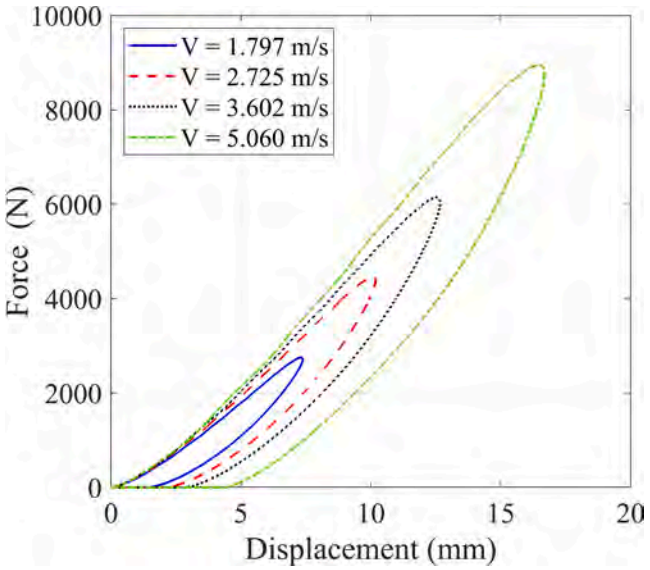

Fig. 10. Numerical force-displacement curves of the impactor in the indentation tests for the four impact velocities, considering the optimized Prony series expansion.

Overall, the final numerical calibration of the TPU-WTR could be considered acceptable, thanks to the improvement achieved in the numerical-experimental correlation of the indentation tests, particularly for the higher impact velocities. It should be also noted that this material model was further tested and validated through the numerical-experimental correlation of the drop-weight tests performed on the foam-filled hexachiral structure described later in Section 2.6.

2.5.2.2. Open-cell polyurethane foam. The CF-45M was numerically modelled through the **LOW DENSITY FOAM* material card available in the software [55]. The low-density foam model is a nonlinear viscoelastic model suitable for specifying strain-rate sensitive behavior of low-density elastomeric foams. This material model requires as input the tabulated experimental results represented by the three stress-strain curves of Fig. 4(b). To simulate the failure behavior of the foam, a tension cutoff stress with elements deletion was used, and this value was set at 14.0 MPa based on the numerical-experimental correlation presented in Section 2.6.

2.5.3. Simplification of the FE model

The preliminary numerical simulations of the foam-filled hexachiral structure turned out to be quite time-consuming. To optimize the design of the recoverable hexachiral structure in a low-energy impact scenario and thus perform numerous FE simulations, as described later in Section 3, a simplification of the FE model was implemented to reduce computational time. The simplification was based on the assumption that the indentation load was applied uniformly across the entire width, i.e., the Z-direction, with reference to Fig. 11(a). This assumption was carefully verified through the numerical-experimental correlation described in Section 2.6. Therefore, only a 1-mm-slice of the FE model was considered, as visible in Fig. 11(b). With this assumption, the numerical impactor had a concentrated mass of 0.182 kg, i.e., the actual mass of 5.457 kg divided by the actual width of the energy absorber, i.e., 30 mm. Furthermore, the 1-mm-slice energy absorber, which was actually 1-finite-element-wide, had the nodes of one side constrained with a Z-symmetry condition, while the nodes of the other side were free to move. For clarity, from here on, the simplified model will be referred to as the "slice" model, as opposed to the "whole" model.

2.6. Numerical-experimental correlation

The numerical-experimental correlation presented here was performed to validate the two FE models of the hexachiral structure, namely, the whole and the slice FE models. The correlation was carried out in two ways: the first was qualitative, examining the overall

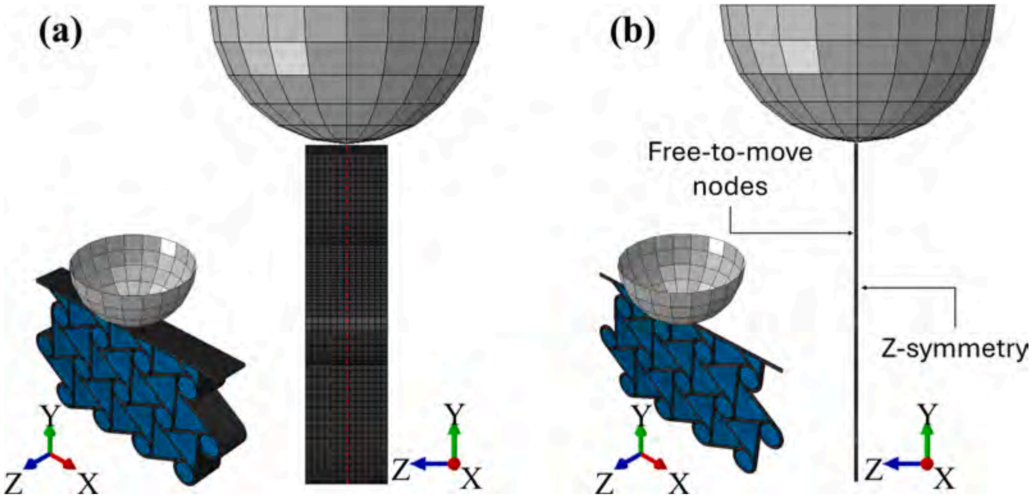

Fig. 11. Isometric and lateral views of the two FE models: (a) whole energy absorber, (b) 1-mm-slice energy absorber.

deformations of the structure, while the second was quantitative, comparing the experimental and numerical force-displacement curves of the impactor. The correlation was done for both the impact velocities, i.e., V1 and V2.

Considering the qualitative correlation, Fig. 12 shows the experimental and numerical deformations of the structure at the maximum indentation of the impactor, just before rebound, i.e., the restitution phase. For the sake of simplicity, only test T1 for impact velocity V1 and test T5 for impact velocity V2 are reported, as the deformations in the other experiments were practically the same. Fig. 12 (a-b) shows the case with impact velocity V1, while Fig. 12 (c-d) shows the case with impact velocity V2. Qualitatively, there were just a few local differences related to the buckling of some ligaments, particularly those located below the area affected by the impact. Overall, the numerical simulations correctly represented the qualitative behavior of the structure for both impact velocities.

The quantitative correlation provided the validation of both the whole and the slice FE models. Fig. 13 shows the experimental and numerical force-displacement curves of the impactor, with the numerical results filtered with a CFC 180 filter. The experimental results in both Fig. 13(a) and Fig. 13 (b) prove the repeatability of the test for each of the two impact velocities, thus confirming the recoverability of the energy absorber for the series of the six impact tests carried out for the present study. The numerical curves of the whole FE model showed consistent trends with those of the experiments, with a well-corresponding peak. Slight differences were found in the restitution phase, attributable to an imperfect calibration of the viscoelastic contribution of both the CF45-M foam and the TPU-WTR filament. The force-displacement curves of the slice FE model can be compared with those of the whole FE model. As shown in Fig. 13(a), the two numerical curves matched perfectly for impact velocity V1, while a slight difference in the peak value was observed for impact velocity V2 (Fig. 13(b)). This was attributed to a different behavior of the shell elements in the final compaction phase of the buckled ligaments, possibly due to the boundary conditions applied in the simplified model.

Further considerations concern the rebound or restitution phase of the impact event [1]. Indeed, the viscoelastic behavior of the structure allowed complete recovery after the impact, but it also induced a rebound effect on the impactor. During the compression phase, the initial kinetic energy, associated solely with the impactor, was partly

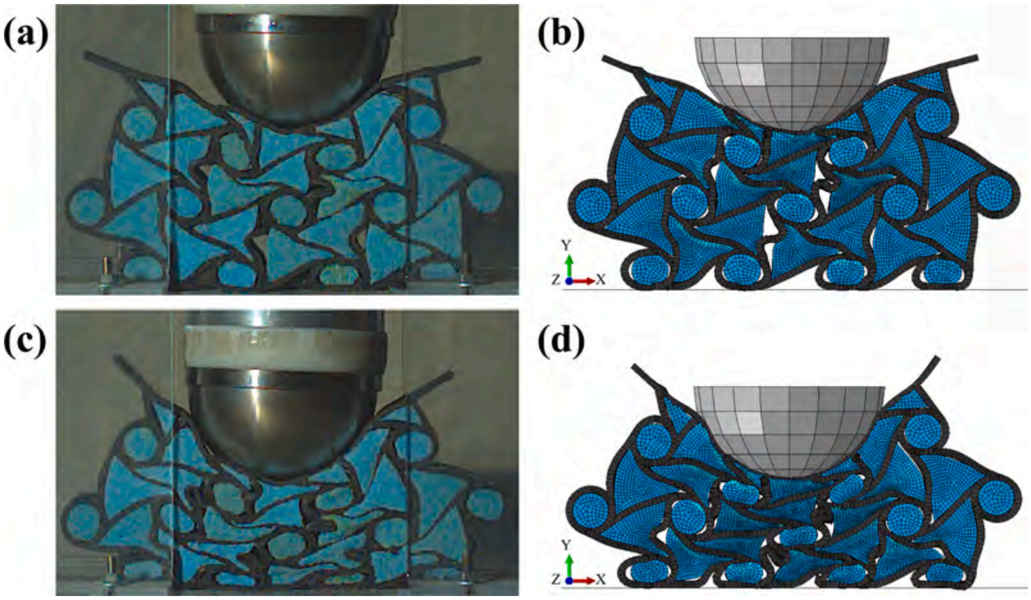

Fig. 12. Deformations of the structure at the impactor maximum indentation, with rendering of shell thickness: (a-b) experiment T1 and whole FE model impacted at V1 = 3.100 m/s, (c-d) experiment T5 and whole FE model impacted at V2 = 5.150 m/s.

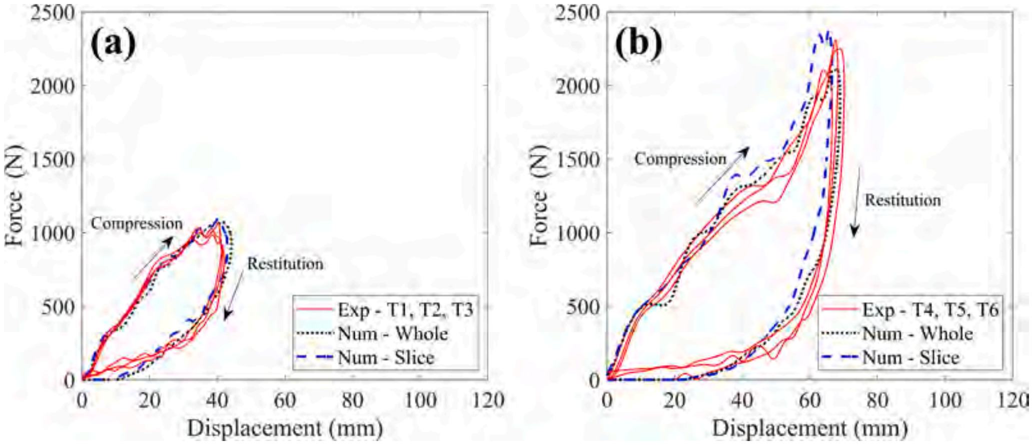

Fig. 13. Comparison between the force-displacement curves of the impactor in the experiments and in the whole and slice FE models: (a) impact velocity V1 = 3.100 m/s, (b) impact velocity V2 = 5.150 m/s. Compression and restitution phases are highlighted.

dissipated and partly transformed into elastic strain energy; thereafter, during the restitution phase, only the elastic strain energy was released and transformed back into kinetic energy of the impactor. With reference to Fig. 13, the amount of energy dissipated in each impact is the area between the curves of the compression and restitution phases. A useful parameter to quantify the rebound effect is the coefficient of restitution *COR*, also denoted by *e*, whose values fall within the range $0 \le e \le 1$: if $e = 1$, the collision is completely elastic, whereas if $e = 0$, the collision is completely inelastic [1]. For an object impacting a stationary target, as in the case of the present study, the coefficient of restitution can be calculated as the ratio of the rebound velocity of the impactor after impact, v_f, to that prior to impact, v_i, as shown in Eq. (1). Thus, *e* is a comparison between the kinetic energy, E_{kin}, of the impactor immediately before impact and that immediately after impact.

$$e = \sqrt{\frac{E_{kin,f}}{E_{kin,\ i}}} = \sqrt{\frac{0.5\cdot m\cdot v_f^2}{0.5\cdot m\cdot v_i^2}} = \frac{v_f}{v_i} \tag{1}$$

Experimental and numerical coefficient of restitutions for the two impact velocities, calculated using Eq. (1), are reported in Table 3. A good correlation between the numerical and experimental values can be observed, thus confirming the quality of the numerical simulations.

Overall, the results of the numerical-experimental correlation indicated that both modelling approaches provided realistic predictions of the response of the foam-filled hexachiral structure in a dynamic indentation test. Furthermore, it was inferred that the assumptions underlying the simplification of the whole FE model, and thus the slice FE model itself, could be considered valid, as the differences were deemed acceptable, especially considering the computational time saved. Indeed, given that all simulations were solved using the Simulia/Abaqus Explicit code in parallel on 25 threads of an Intel(R) Xeon(R) Gold 6338 CPU @ 2.00 GHz, the slice FE model in the case of impact velocity V1 required 16% of the time of the whole FE model (13 min vs 79 min), and in the case of impact velocity V2, the slice FE model required 15% of the time of the whole FE model (14 min vs 94 min).

Table 3
Experimental and numerical coefficient of restitutions.

	Impact velocity V1			Impact velocity V2		
	v_i (m/s)	v_f (m/s)	e (-)	v_i (m/s)	v_f (m/s)	e (-)
Average of experiments	3.100	1.8097	0.58	5.150	2.3423	0.45
Whole FE model	3.100	1.6381	0.53	5.150	2.3651	0.46
Slice FE model	3.100	1.7161	0.55	5.150	2.3534	0.46

3. Engineering application of the energy absorber in a crash scenario

A potential engineering application of the recoverable foam-filled hexachiral structure is hereby considered, focusing on a simplified scenario selected to be representative of a low-energy impact between a vehicle bumper and a pedestrian (a typical VRU). Numerous studies in the literature analyze in detail the response of vehicle front-end systems, for example in [38,40,41,58]. In the present work, it was decided to prove the design flexibility of the concept of this type of recoverable energy absorber by conducting analyses using simpler and plausible conditions. The EEVC/WG17 EURO Phase 2 regulation [59] and the Regulation (EC) No 78/2009 — Annex I, Section 3.1(a) [60] provide specific requirements and load conditions for pedestrian lower extremity safety. These regulations were used to define the impact conditions and limit force requirements.

The study was conducted adopting the numerical technique of surrogate models, also known as metamodels, built with regression models, which allowed the optimization procedure to be performed more quickly using a genetic algorithm. The application of this methodology has proven effective in many cases, including the design of vehicle bumpers, as explained in the review reported in [61] and demonstrated with practical examples in [37,44,62]. Surrogate models can provide an approximate functional relationship to relate design variables to a specific objective with a moderate number of full numerical simulations.

3.1. Description of the design optimization problem

The design optimization problem consisted of the impact of a cylindrical impactor, with geometry and mass representative of a lower legform of a pedestrian, against a portion of a foam-filled hexachiral energy absorber. Although in the real crash scenario the legform is deformable and contributes to energy absorption and force limitation, a conservative simplified approach was adopted by considering a rigid impactor with a concentrated mass of 12 kg, a diameter of 100 mm, and an impact velocity of 9 m/s (or 32.4 km/h). As regards the geometrical parameters of the energy absorber (listed in Table 1), the global dimensions were set as fixed variables, i.e., 300 × 100 × 150 mm^3 ($LA \times WA \times HA$), while the thicknesses of chiral ligaments (t_L), chiral nodes (t_N) and boundary skin (t_B) as well as the number of cells in X-axis (Nx) and the characteristic L/r ratio were considered as the design variables of the problem. An example of such a whole FE model is shown in Fig. 14 (a). The width of the energy absorber, as well as the diameter and mass of the cylindrical impactor, were similar to the typical vehicle front bumper [37,40,41] and lower legform [59], respectively. The height *HA* is higher than the typical distance between the external surface of a

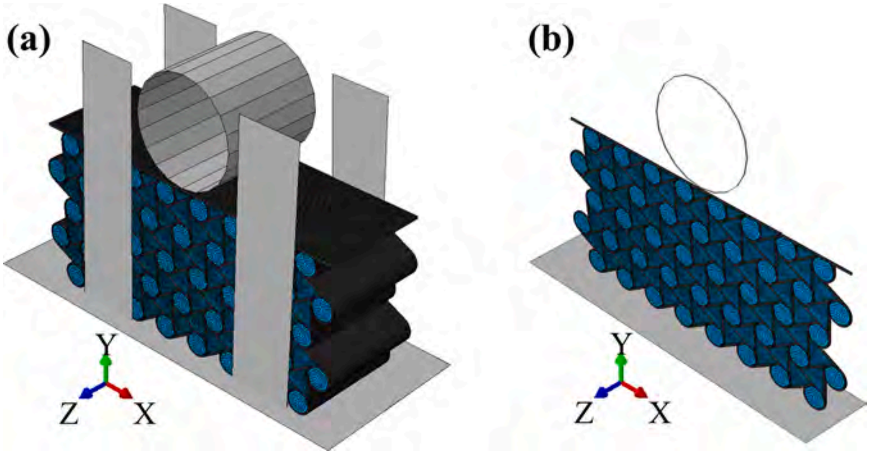

Fig. 14. Example of FE model adopted in design optimization problem: (a) whole FE model, (b) slice FE model.

bumper and the rigid beam that represents its primary structure, in connection with the car chassis. However, the scope of the optimization was the minimization of the indentation required to fulfil an equivalent injury criterion in the simplified scenario, so to provide a first assessment related to the possibility of an effective installation of the recoverable system, with minimal modification of the configurations adopted in the automotive field. Finally, with regard to the duration of the simulated impact event, it was set at 0.07 s.

The optimization was actually performed on the slice FE model, to reduce computational time. The adequacy of such reduced model to represent the wider absorber was validated in Section 2.6. Hence, slice FE models were adopted to construct the metamodels and conduct the design optimization, resulting in a significant reduction in computational time. Accordingly, the numerical impactor width was reduced to 1 mm and a mass of 0.12 kg was considered, corresponding to the actual mass divided by the actual width of the energy absorber. An example of the slice FE model is shown in Fig. 14(b).

Concerning the injury criterion, the regulations [59,60] prescribe a maximum acceleration measured at the upper end of the tibia (Acc_{Limit}) not exceeding 170 g. In the simplified scenario considered, a force limit of 13 kN was selected for the 12 kg rigid mass impactor ($m_{impactor}$), corresponding to an acceleration value of approximately 110 g, thus providing a safety factor (SF) of about 1.54 on the regulation value. Consequently, the force limit per unit width (F_{Limit}) considered in the slice FE model was 130 N/mm. The relationship between F_{Limit} and Acc_{Limit} is illustrated in the following Eq. (2):

$$\begin{aligned} F_{Limit} &= \frac{(Acc_{Limit}/SF)\cdot m_{impactor}}{WA} \\ &= \frac{(170\ g/1.54)\cdot 9.81\ m/s^2\cdot 12\ kg}{100\ mm} = 130\ N\Big/mm \end{aligned} \tag{2}$$

The main objective of the design optimization was to identify the geometrical parameters of the foam-filled hexachiral structure, i.e., the five design variables (Nx, L/r, t_L, t_N, t_B), that minimize the maximum indentation (δ_{max}) of the impactor and simultaneously limit the maximum force (F_{max}) exerted on the impactor. This objective, related to the indentation with force limitation, was chosen because these two quantities are generally in conflict in the design of an energy absorber.

3.2. Setup of the design optimization problem: metamodels and genetic algorithm

The parametric slice FE model was used to build a dataset for the training of two surrogate models, or metamodels. A Latin hypercube sampling (LHS) was used to generate 200 well-distributed samples, i.e., combinations of the five design variables, given the lower and upper bounds reported in Table 4. These bounds were consistent with those adopted in [16] and were related to technological limitations. Subsequently, 200 Abaqus FE simulations were performed. Several simulations were not completed due to numerical issues and were not used to train the metamodels. Eventually, 137 simulations were considered reliable to estimate the impactor maximum indentation (δ_{max}) and the impactor maximum force (F_{max}), which were stored and then added to the dataset.

The Matlab® Regression Learner App [57] was used to train, validate, and test two metamodels. Among the available regression models, the Matérn 5/2 Gaussian process regression (GPR) was employed to construct two distinct metamodels, as it proved to be the most accurate. Specifically, the first metamodel was used to predict the impactor maximum indentation by giving the five geometrical parameters as predictors, whereas the latter was used to predict the impactor maximum force by giving the five geometrical parameters and the maximum indentation as predictors. For this latter metamodel, adding maximum indentation as a predictor increased accuracy.

The two distinct metamodels, constructed with a Matérn 5/2 GPR, were trained on 90% of the 137 samples, with validation performed using a 5-fold cross-validation scheme to prevent overfitting, and finally tested on the reserved 10% of the 137 samples not used for training and validation. The validation and testing metrics of the two metamodels are reported in Table 5. To allow for a better comparability of the metamodels, the normalized root mean square error ($NRMSE$) was provided, calculated as the $RMSE$ divided by a normalization factor represented by the range of the true response, i.e., the difference between maximum (y_{max}) and minimum (y_{min}) values of the parameter under consideration, as reported in Eq. (3):

$$NRMSE = \frac{RMSE}{y_{max} - y_{min}}\cdot 100 \tag{3}$$

Both the validation and the testing metrics reported in Table 5, as well as the correlations between predicted and sample responses visible in Fig. 15, confirm that the metamodels can be considered reasonably accurate, and thus usable for an efficient optimization procedure using a genetic algorithm.

The optimization of the foam-filled hexachiral structure was performed having the objective of minimizing the maximum indentation of

Table 4
Lower and upper bounds of the five design variables (Nx allowed integer values only).

Design variable	Nx (-)	L/r (-)	t_L (mm)	t_N (mm)	t_B (mm)
Lower bound	2	2	0.8	0.8	0.8
Upper bound	8	10	3	3	3

Table 5
Metrics of the two metamodels.

Metamodel	Number of predictors	Validation			Testing		
		RMSE	*NRMSE*	R^2	*RMSE*	*NRMSE*	R^2
Impactor max indentation, δ_{max}	5	1.81 mm	2.61%	0.99	2.54 mm	3.66%	0.97
Impactor max force, F_{max}	6	12.86 N	8.32%	0.87	13.09 N	8.47%	0.85

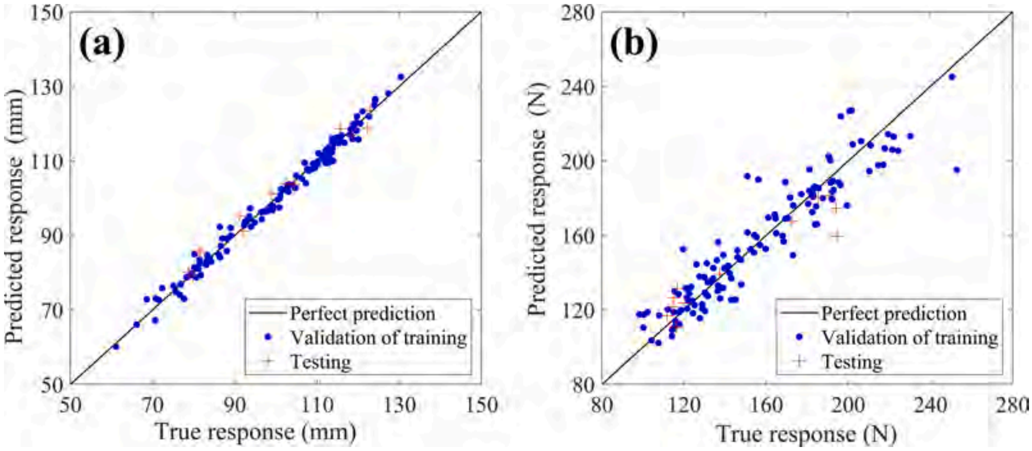

Fig. 15. Predicted vs true response: (a) impactor maximum indentation, (b) impactor maximum force.

the impactor and simultaneously limiting the maximum force applied on the impactor. The mathematical model is defined in Eq. (4), and the Matlab® function *ga* [57] was adopted to solve this constrained single-objective optimization problem using the two constructed metamodels. The control parameters adopted to obtain the results are indicated in Table 6. In addition to the force constraint, a linear constraint and a non-linear constraint were imposed: the former considered the thicknesses t_L and t_N and was due to how the FE model was generated, while the latter considered the diameter of the cylindrical foam inserts ($D_{cylinder}$) and was due to manufacturing reasons.

$$
\left\{
\begin{array}{ll}
Minimize & \delta_{max}(Nx, L/r,\ t_L,\ t_N,\ t_B) \\
s.t. & \left\{
\begin{array}{c}
2 \le Nx \le 8 \\
2 \le L/r \le 10 \\
0.8\ mm \le t_L \le 3\ mm \\
0.8\ mm \le t_N \le 3\ mm \\
0.8\ mm \le t_B \le 3\ mm \\
F_{max}(\delta_{max}) \le 130\ N \\
t_N \ge t_L/2 \\
D_{cylinder}(Nx, L/r,\ t_L,\ t_N) \ge 10\ mm
\end{array}
\right.
\end{array}
\right.
\tag{4}
$$

3.3. *Results of the optimization problem*

The optimal combination of the five design variables obtained from the constrained optimization problem is reported in Table 7, along with the corresponding predicted maximum indentation and maximum force of the impactor. This optimum is shown in Fig. 16 together with the dataset values, which highlight the effect of the five design variables on the impactor's maximum indentation. Looking at the trend for each design variable in the range considered, the indentation δ_{max} was more sensitive to three design variables, namely *Nx*, *L/r*, and t_L, than to the other two, namely t_N and t_B. Furthermore, as shown in Fig. 17, the optimum was found exactly on the boundary of the feasible region related to the force constraint: this optimal geometrical configuration was characterized by a very satisfactory performance with a maximum indentation significantly lower than most samples of the dataset, thus confirming the high design flexibility of this foam-filled hexachiral structure concept. According to Fig. 17, the F_{max}-δ_{max} dataset confirms the existing conflict between the minimization of indentation and the limitation of the force, as it would be expected in the design of an energy absorber. It can therefore be said that if a high indentation is desired, which means having a more compliant energy absorber, then there is a risk of obtaining high force levels due to the compaction of the structure; on the other hand, if indentation is to be limited, there is a risk of high force levels due to the fact that the impactor strikes a more rigid energy absorber.

In addition to the optimal values, Table 7 reports the result of the slice FE model simulation, which was performed to verify the optimization result. From the table, the relative errors for δ_{max} and F_{max} between the optimization and FE simulation results are 1.98% and 9.74%, respectively. These values were due to the quality of the two metamodels, and they were consistent with the validation and testing errors reported in Table 5. It could therefore be concluded that the constrained optimization exploiting the two metamodels was able to find a solution

Table 6
Control parameters of the genetic algorithm.

Parameter	Value
Population size	50
Max number of generations	100
Crossover fraction	0.25
Elitism	Implemented

Table 7
Optimization results and corresponding slice FE model results.

	Nx (-)	*L/r* (-)	t_L (mm)	t_N (mm)	t_B (mm)	δ_{max} (mm)	F_{max} (N)
Optimization	6	3.32	2.51	2.49	1.87	68.42	129.98
FE simulation						69.80	144.00
Relative error						1.98%	9.74%

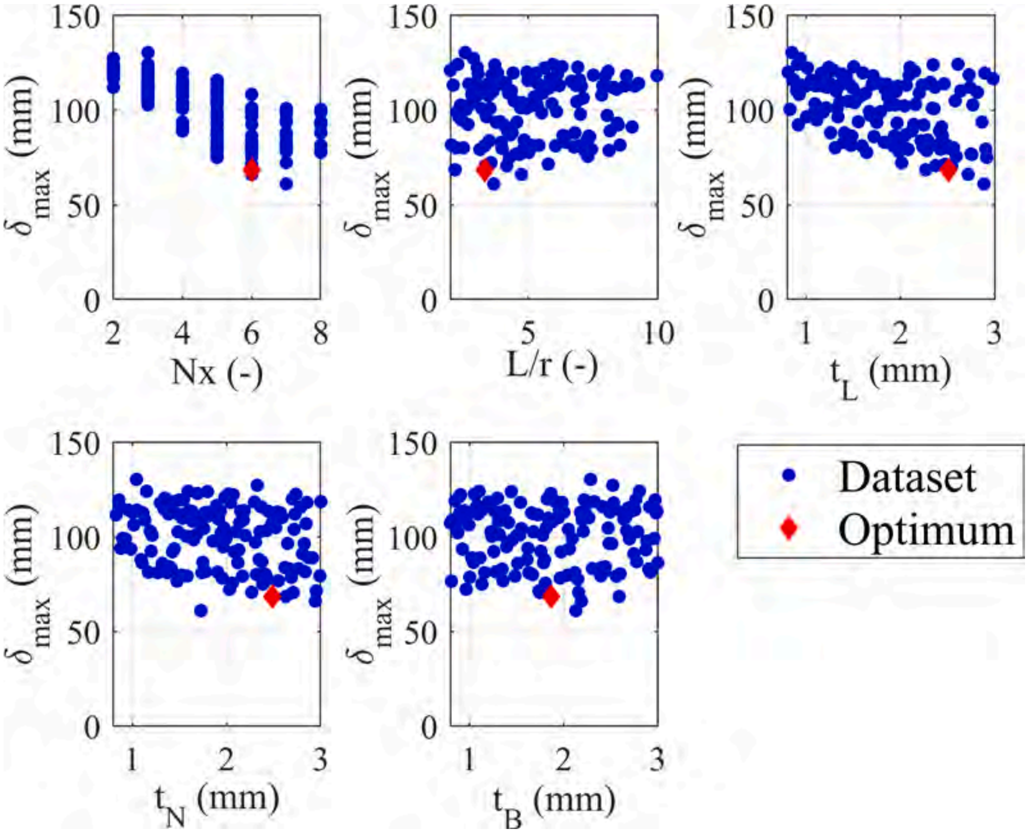

Fig. 16. Dataset values: effect of the five design variables on the impactor maximum indentation. The optimization result is also reported.

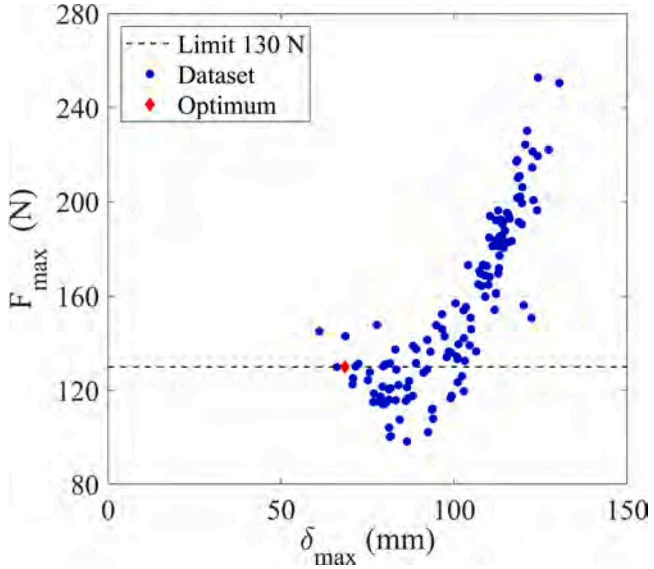

Fig. 17. Dataset values: impactor maximum force vs impactor maximum indentation. The feasible region for the genetic algorithm was below the 130 N limit.

that met all requirements, and that the actual correctness of the solution could be improved by increasing the quality of the metamodels, for example, by considering a much larger number of samples for the training. Finally, it is worth noting that the value F_{max} of the FE simulation exceeded the imposed limit of 130 N, but this solution remained below the threshold imposed by the regulations, thanks to the safety margin defined initially, as clearly visible in the force-displacement curve of the impactor obtained from the simulation on the slice FE model, shown in Fig. 18(a). The optimized foam-filled hexachiral structure and its deformation at the impactor maximum indentation are shown in Fig. 19. The whole structure contributed to the absorption of the energy, and the auxetic effect of the structure prevented the foam from flowing away from the impact zone. The average density of the optimal absorber was approximately 562 kg/m^3. The total mass was 2679 g, of which 2415 g was TPU-WTR and 264 g was CF-45 M. The foam volume fraction was about 56% of the structure's total volume.

The last consideration, regarding this optimal configuration, concerned the coefficient of restitution that permitted to quantify the rebound effect, as described in Section 2.6. With reference to Fig. 18(a), the amount of energy dissipated was the area between the two curves of the compression and restitution phases, while, with reference to Fig. 18 (b) showing the velocity of the impactor, the coefficient of restitution e was 0.44, evaluated using Eq. (1). Overall, this could be an interesting property for a recoverable vehicle bumper since the geometrical design variables of the energy absorber could be tuned to minimize the rebound effect on the VRU.

4. Conclusions

This work presented a recoverable composite energy absorber based on a foam-filled hexachiral auxetic structure, designed to mitigate injuries in a representative low-energy impact scenario involving pedestrians. The viscoelastic absorber consisted of a 3D-printed auxetic frame made of thermoplastic polyurethane with waste tire rubber (TPU-WTR) and a strain-rate sensitive polyurethane foam filling (CF45-M). Its working principle relied on the synergistic interaction between the auxetic frame and the foam, which enhanced energy dissipation, stabilized deformation, and enabled full structural recovery after impact.

A prototype of the energy absorber was manufactured and subjected to mechanical characterization and drop-weight impact tests. These

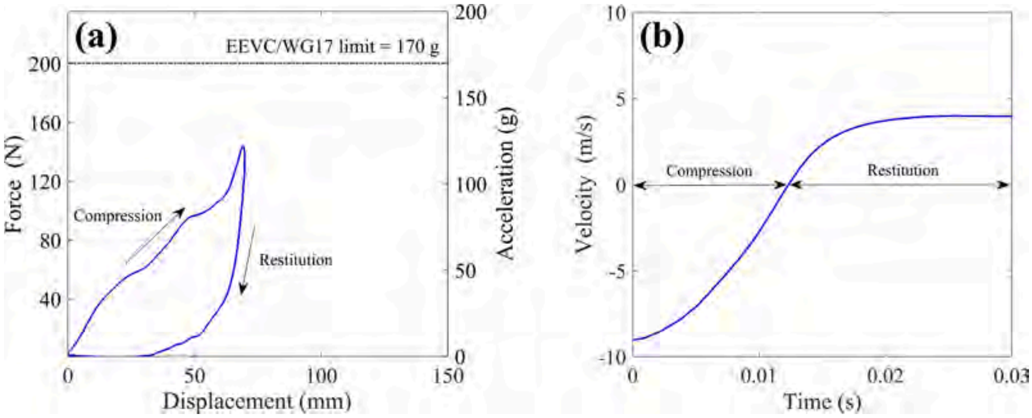

Fig. 18. Impactor response resulting from the simulation on the slice FE model with optimal results: (a) force-displacement curve, with the peak of the curve clearly below the limit imposed by the regulations, (b) velocity of the impactor. Compression and restitution phases are highlighted.

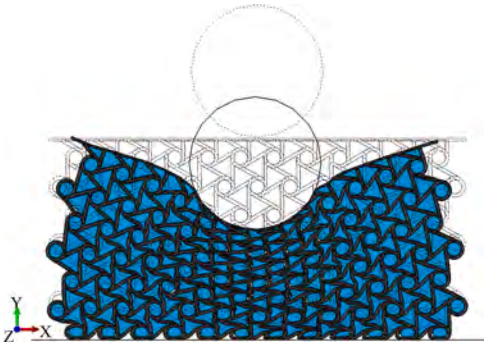

Fig. 19. Deformation of the optimal structure at the impactor maximum indentation just before the rebound, with rendering of shell thickness. The undeformed shape is superimposed.

experiments confirmed the repeatability of the performance of the absorber and validated its recoverability. Finite element models were developed and calibrated using experimental data, accurately reproducing the responses observed during the testing activity. The appreciable numerical-experimental correlation was achieved after identifying, through a series of experimental tests, the material models, such as the visco-hyperelastic model adopted for the TPU-WTR, which combines an Odgen hyperelastic model and a generalized Maxwell viscous model.

The validated numerical approach was used to build a dataset of responses depending on geometrical parameters, and then the dataset was used to train and validate two surrogate models based on Gaussian process regression enabling efficient exploration of the design space. A genetic optimization procedure, performed with such surrogate models, proved effective in finding the optimal configuration of the energy absorber that minimized indentation while keeping the peak force within the imposed limits. The auxetic configuration prevented foam from flowing and improved global stability during impact, with the rebound effect quantified by a coefficient of restitution of approximately 0.44.

From this work, some general considerations could be made about the design and application of recoverable auxetic absorbers:

- The viscoelastic combination of auxetic frame and PU foam effectively mitigated the limitations of each constituent, providing both energy absorption and recoverability.
- Optimization using metamodels significantly reduced computational cost compared to full FE simulations, though accuracy depended on the quality of the metamodels.
- The rebound effect requires further investigation to assess its influence on pedestrian safety and to develop strategies to mitigate it.

Despite the limitations represented by the simplified crash assumptions, these findings highlighted the potential of the concept to design reusable absorbers for advanced low-energy impact protection systems.

Declaration of generative AI and AI-assisted technologies in the manuscript preparation process

During the preparation of this work the authors used GPT-5 in order to improve readability, grammar, and language. After using this tool, the authors reviewed and edited the content as needed and take full responsibility for the content of the published article.

CRediT authorship contribution statement

Sebastiano Di Mauro: Writing – original draft, Visualization, Validation, Software, Investigation, Formal analysis, Data curation, Conceptualization. **Nejc Novak:** Writing – review & editing, Supervision, Methodology. **Serena Graziosi:** Writing – review & editing, Supervision, Resources, Conceptualization. **Raffaele Pugliese:** Resources, Methodology. **Alessandro Galbiati:** Software. **Alessandro Gadola:** Investigation. **Alessandro Airoldi:** Supervision, Project administration, Methodology, Funding acquisition, Conceptualization.

Declaration of competing interest

The authors declare that they have no known competing financial interests or personal relationships that could have appeared to influence the work reported in this paper.

Acknowledgements

This study was carried out within the MOST - Sustainable Mobility National Research Center and received funding from the European Union Next-Generation EU (Piano Nazionale di Ripresa e Resilienza (PNRR) - Missione 4. Componente 2, Investimento 1.4 - D.D. 1033 17/06/2022, CN00000023). This manuscript reflects only the authors' views and opinions, neither the European Union nor the European Commission can be considered responsible for them.

The authors acknowledge the Slovenian Research and Innovation Agency's financial support of the national research program funding No. P2-0063 and basic research project No. J2-60049.

Finally, the authors also wish to acknowledge Diego Di Brizzi (Politecnico di Milano) for the support in the design and parameterization of the hexachiral auxetic structure.

Data availability

Data will be made available on request.

References

[1] G. Lu, T.X. Yu, Energy Absorption of Structures and Materials, Elsevier, 2003.

[2] H. Yin, W. Zhang, L. Zhu, F. Meng, J. Liu, G. Wen, Review on lattice structures for energy absorption properties, Compos. Struct. 304 (2023) 116397, https://doi.org/10.1016/j.compstruct.2022.116397.

[3] N. Novak, M. Vesenjak, Z. Ren, Auxetic Cellular materials - a review, Strojniški Vestnik – J. Mech. Eng. 62 (2016) 485–493, https://doi.org/10.5545/sv-jme.2016.3656.

[4] X. Ren, R. Das, P. Tran, T.D. Ngo, Y.M. Xie, Auxetic metamaterials and structures: a review, Smart Mater. Struct. 27 (2018) 023001, https://doi.org/10.1088/1361-665X/aaa61c.

[5] X. Xue, C. Lin, F. Wu, Z. Li, J. Liao, Lattice structures with negative Poisson's ratio: a review, Mater. Today Commun. 34 (2023) 105132, https://doi.org/10.1016/j.mtcomm.2022.105132.

[6] X. Li, W. Peng, W. Wu, J. Xiong, Y. Lu, Auxetic mechanical metamaterials: from soft to stiff, Int. J. Extrem. Manuf. 5 (2023) 042003, https://doi.org/10.1088/2631-7990/ace668.

[7] A.S. Shuaibu, J. Deng, C. Xu, V.P. Ade-Oke, A. Aliyu, D. Momoh, Advancing auxetic materials: emerging development and innovative applications, Rev. Adv. Mater. Sci. 63 (2024), https://doi.org/10.1515/rams-2024-0021, 2024.

[8] Y. Zhang, W.Z. Jiang, W. Jiang, X.Y. Zhang, J. Dong, Y.M. Xie, K.E. Evans, X. Ren, Recent advances of auxetic metamaterials in smart materials and structural systems, Adv. Funct. Mater. (2025) 2421746, https://doi.org/10.1002/adfm.202421746 n/a.

[9] A. Alderson, K.L. Alderson, D. Attard, K.E. Evans, R. Gatt, J.N. Grima, W. Miller, N. Ravirala, C.W. Smith, K. Zied, Elastic constants of 3-, 4- and 6-connected chiral and anti-chiral honeycombs subject to uniaxial in-plane loading, Compos. Sci. Technol. 70 (2010) 1042–1048, https://doi.org/10.1016/j.compscitech.2009.07.009.

[10] Y. Jiang, B. Rudra, J. Shim, Y. Li, Limiting strain for auxeticity under large compressive deformation: chiral vs. re-entrant cellular solids, Int. J. Solids Struct. 162 (2019) 87–95, https://doi.org/10.1016/j.ijsolstr.2018.11.035.

[11] A. Mauko, Y. Yilmaz, N. Novak, T. Doktor, M. Vesenjak, Z. Ren, Dynamic characterisation of novel three-dimensional axisymmetric chiral auxetic structure, Compos. Struct. 333 (2024) 117949, https://doi.org/10.1016/j.compstruct.2024.117949.

[12] L.L. Hu, M.Zh. Zhou, H. Deng, Dynamic indentation of auxetic and non-auxetic honeycombs under large deformation, Compos. Struct. 207 (2019) 323–330, https://doi.org/10.1016/j.compstruct.2018.09.066.

[13] F. Usta, H.S. Türkmen, F. Scarpa, Low-velocity impact resistance of composite sandwich panels with various types of auxetic and non-auxetic core structures, Thin-Walled Struct. 163 (2021) 107738, https://doi.org/10.1016/j.tws.2021.107738.

[14] R.P. Bohara, S. Linforth, T. Nguyen, A. Ghazlan, T. Ngo, Anti-blast and -impact performances of auxetic structures: a review of structures, materials, methods, and fabrications, Eng. Struct. 276 (2023) 115377, https://doi.org/10.1016/j.engstruct.2022.115377.

[15] S. Yang, C. Qi, D. Wang, R. Gao, H. Hu, J. Shu, A comparative study of ballistic resistance of sandwich panels with aluminum foam and auxetic honeycomb cores, Adv. Mech. Eng. 2013 (2015), https://doi.org/10.1155/2013/589216.

[16] A. Airoldi, N. Novak, F. Sgobba, A. Gilardelli, M. Borovinšek, Foam-filled energy absorbers with auxetic behaviour for localized impacts, Mater. Sci. Eng. A 788 (2020) 139500, https://doi.org/10.1016/j.msea.2020.139500.

[17] C. Chen, A. Airoldi, A.M. Caporale, G. Sala, X. Yin, Impact response of composite energy absorbers based on foam-filled metallic and polymeric auxetic frames, Compos. Struct. 331 (2024) 117916, https://doi.org/10.1016/j.compstruct.2024.117916.

[18] T. Li, Y. Chen, X. Hu, Y. Li, L. Wang, Exploiting negative Poisson's ratio to design 3D-printed composites with enhanced mechanical properties, Mater. Des. 142 (2018) 247–258, https://doi.org/10.1016/j.matdes.2018.01.034.

[19] T. Li, F. Liu, L. Wang, Enhancing indentation and impact resistance in auxetic composite materials, Compos. Part B: Eng. 198 (2020) 108229, https://doi.org/10.1016/j.compositesb.2020.108229.

[20] H.C. Luo, X. Ren, Y. Zhang, X.Y. Zhang, X.G. Zhang, C. Luo, X. Cheng, Y.M. Xie, Mechanical properties of foam-filled hexagonal and re-entrant honeycombs under uniaxial compression, Compos. Struct. 280 (2022) 114922, https://doi.org/10.1016/j.compstruct.2021.114922.

[21] N. Novak, H. Al-Rifaie, A. Airoldi, L. Krstulović-Opara, T. Łodygowski, Z. Ren, M. Vesenjak, Quasi-static and impact behaviour of foam-filled graded auxetic panel, Int. J. Impact Eng. 178 (2023) 104606, https://doi.org/10.1016/j.ijimpeng.2023.104606.

[22] S. Ghoddousi, A.V. Yakhforvazan, M. Safarabadi, Effects of foam filling on flexural performance of 3D printed chiral honeycombs, Thin-Walled Struct. 209 (2025) 112893, https://doi.org/10.1016/j.tws.2024.112893.

[23] Q. Hu, X. Zhang, J. Zhang, G. Lu, K.M. Tse, A review on energy absorption performance of auxetic composites with fillings, Thin-Walled Struct. 205 (2024) 112348, https://doi.org/10.1016/j.tws.2024.112348.

[24] J. Fan, L. Zhang, S. Wei, Z. Zhang, S.-K. Choi, B. Song, Y. Shi, A review of additive manufacturing of metamaterials and developing trends, Mater. Today 50 (2021) 303–328, https://doi.org/10.1016/j.mattod.2021.04.019.

[25] N. Novak, L. Biasetto, P. Rebesan, F. Zanini, S. Carmignato, L. Krstulović-Opara, M. Vesenjak, Z. Ren, Experimental and computational evaluation of tensile properties of additively manufactured hexa- and tetrachiral auxetic cellular structures, Addit. Manuf. 45 (2021) 102022, https://doi.org/10.1016/j.addma.2021.102022.

[26] S.D. Papka, S. Kyriakides, In-plane compressive response and crushing of honeycomb, J Mech. Phys. Solids 42 (1994) 1499–1532, https://doi.org/10.1016/0022-5096(94)90085-X.

[27] S.R. Reid, Plastic deformation mechanisms in axially compressed metal tubes used as impact energy absorbers, Int. J. Mech. Sci. 35 (1993) 1035–1052, https://doi.org/10.1016/0020-7403(93)90054-X.

[28] F. Rahimidehgolan, W. Altenhof, Compressive behavior and deformation mechanisms of rigid polymeric foams: a review, Compos. Part B: Eng. 253 (2023) 110513, https://doi.org/10.1016/j.compositesb.2023.110513.

[29] K. Bertoldi, Harnessing instabilities to design tunable architected cellular materials, Annu. Rev. Mater. Res. 47 (2017) 51–61, https://doi.org/10.1146/annurev-matsci-070616-123908.

[30] L.R. Meza, S. Das, J.R. Greer, Strong, lightweight, and recoverable three-dimensional ceramic nanolattices, Science (2014), https://doi.org/10.1126/science.1255908.

[31] L. Salari-Sharif, T. Schaedler, L. Valdevit, Energy dissipation mechanisms in hollow metallic microlattices, J. Mater. Res. 29 (2014) 1755–1770, https://doi.org/10.1557/jmr.2014.226.

[32] D.M. Correa, T. Klatt, S. Cortes, M. Haberman, D. Kovar, C. Seepersad, Negative stiffness honeycombs for recoverable shock isolation, Rapid Prototyp. J. 21 (2015) 193–200, https://doi.org/10.1108/RPJ-12-2014-0182.

[33] D. Restrepo, N.D. Mankame, P.D. Zavattieri, Phase transforming cellular materials, Extreme Mech. Lett. 4 (2015) 52–60, https://doi.org/10.1016/j.eml.2015.08.001.

[34] S. Shan, S.H. Kang, J.R. Raney, P. Wang, L. Fang, F. Candido, J.A. Lewis, K. Bertoldi, Multistable architected materials for trapping elastic strain energy, Adv. Mater. 27 (2015) 4296–4301, https://doi.org/10.1002/adma.201501708.

[35] X. Yao, K. Liu, Q. Dong, X. Li, C. Ma, N. Hu, Tunable and recoverable energy absorption of foam-embedded architected cellular composite material at multiple strain rates, Compos. Struct. 329 (2024) 117745, https://doi.org/10.1016/j.compstruct.2023.117745.

[36] M. Seyedkazemi, H. Wenqi, G. Jing, P. Ahmadi, A. Khajehdezfuly, Auxetic structures with viscoelastic behavior: a review of mechanisms, simulation, and future perspectives, Structures 70 (2024) 107610, https://doi.org/10.1016/j.istruc.2024.107610.

[37] Z. Xiao, J. Fang, G. Sun, Q. Li, Crashworthiness design for functionally graded foam-filled bumper beam, Adv. Eng. Softw. 85 (2015) 81–95, https://doi.org/10.1016/j.advengsoft.2015.03.005.

[38] G. Zhou, Z.-D. Ma, G. Li, A. Cheng, L. Duan, W. Zhao, Design optimization of a novel NPR crash box based on multi-objective genetic algorithm, Struct. Multidisc. Optim. 54 (2016) 673–684, https://doi.org/10.1007/s00158-016-1452-z.

[39] C. Wang, Y. Li, W. Zhao, S. Zou, G. Zhou, Y. Wang, Structure design and multi-objective optimization of a novel crash box based on biomimetic structure, Int. J. Mech. Sci. 138–139 (2018) 489–501, https://doi.org/10.1016/j.ijmecsci.2018.01.032.

[40] C. Wang, W. Wang, W. Zhao, Y. Wang, G. Zhou, Structure design and multi-objective optimization of a novel NPR bumper system, Compos. Part B: Eng. 153 (2018) 78–96, https://doi.org/10.1016/j.compositesb.2018.07.024.

[41] S. Yang, Y. Sun, C. Qi, Performance assessment and optimal design of hybrid material bumper for pedestrian lower extremity protection, Int. J. Mech. Sci. 165 (2020) 105210, https://doi.org/10.1016/j.ijmecsci.2019.105210.

[42] F. Ma, H. Liang, Y. Pu, Q. Wang, Y. Zhao, Multi-objective optimization of crash box filled with three-dimensional cellular structure under multi-angle impact loading, Proc. Instit. Mech. Eng. Part D: J. Autom. Eng. 235 (2021) 2397–2412, https://doi.org/10.1177/0954407021998174.

[43] Z. Song, H. Liang, H. Ding, M. Ma, Structure design and mechanical properties of a novel anti-collision system with negative Poisson's ratio core, Int. J. Mech. Sci. 239 (2023) 107864, https://doi.org/10.1016/j.ijmecsci.2022.107864.

[44] H. Tan, Z. He, E. Li, A. Cheng, T. Chen, X. Tan, Q. Li, B. Xu, Crashworthiness design and multi-objective optimization of a novel auxetic hierarchical honeycomb crash box, Struct. Multidisc. Optim. 64 (2021) 2009–2024, https://doi.org/10.1007/s00158-021-02961-9.

[45] Y. Zhu, Z.-P. Wang, L.H. Poh, Auxetic hexachiral structures with wavy ligaments for large elasto-plastic deformation, Smart Mater. Struct. 27 (2018), https://doi.org/10.1088/1361-665X/aab33d.

[46] A. Montazeri, E. Bahmanpour, M. Safarabadi, Three-point bending behavior of foam-filled conventional and auxetic 3D-printed honeycombs, Adv. Eng. Mater. 25 (2023) 2300273, https://doi.org/10.1002/adem.202300273.

[47] S. Badini, S. Graziosi, M. Carboni, S. Regondi, R. Pugliese, Sustainable 3D printing with recycled tire rubber-based filaments: an investigation of process parameters and mechanical behaviour, RPJ 30 (2024) 571–587, https://doi.org/10.1108/RPJ-08-2023-0309.

[48] M.C. Boyce, E.M. Arruda, Constitutive Models of Rubber Elasticity: A Review, ResearchGate (n.d.). https://www.researchgate.net/publication/273006102_Constitutive_Models_of_Rubber_Elasticity_A_Review.

[49] A. Airoldi, S. Fournier, E. Borlandelli, P. Bettini, G. Sala, Design and manufacturing of skins based on composite corrugated laminates for morphing aerodynamic surfaces, Smart Mater. Struct. 26 (2017) 045024, https://doi.org/10.1088/1361-665X/aa6069.

[50] Abaqus Documentation - SIMULIA, (2023).

[51] B. Pinedo, M. Hadfield, I. Tzanakis, M. Conte, M. Anand, Thermal analysis and tribological investigation on TPU and NBR elastomers applied to sealing applications, Tribol. Int. 127 (2018) 24–36, https://doi.org/10.1016/j.triboint.2018.05.032.

[52] J. Bergström, 6 - Linear viscoelasticity, in: J. Bergström (Ed.), Mechanics of Solid Polymers, William Andrew Publishing, 2015, pp. 309–351, https://doi.org/10.1016/B978-0-323-31150-2.00006-6.

[53] Abaqus materials guide - SIMULIA, (2023).

[54] G. Yang, H. Wu, H. Dong, F. Huang, Compressive behavior and visco-hyperelastic constitutive of polyurethane elastomer over a wide range of strain rates, Polym. Test. 138 (2024) 108553, https://doi.org/10.1016/j.polymertesting.2024.108553.

[55] Abaqus keywords guide - SIMULIA, (2023).

[56] F. Pelayo, D. Blanco, P. Fernández, J. González, N. Beltrán, Viscoelastic behaviour of flexible thermoplastic polyurethane additively manufactured parts: influence of inner-structure design factors, Polymers 13 (2021) 2365, https://doi.org/10.3390/polym13142365.

[57] MATLAB documentation R2023b - The MathWorks Inc., (2023).

[58] A. Scattina, F. Mo, C. Masson, M. Avalle, P.J. Arnoux, Analysis of the influence of passenger vehicles front-end design on pedestrian lower extremity injuries by means of the LLMS model, Traffic Inj. Prev. 19 (2018) 535–541, https://doi.org/10.1080/15389588.2018.1432858.

[59] EEVC, EEVC Working Group 17 report: improved test methods to evaluate pedestrian protection afforded by passenger cars, in: 2002.

[60] Regulation (EC) No 78/2009 of the European Parliament and of the Council of 14 January 2009 on the type-approval of motor vehicles with regard to the protection of pedestrians and other vulnerable road users, amending Directive 2007/46/EC and repealing directives 2003/102/EC and 2005/66/EC (Text with EEA relevance). http://data.europa.eu/eli/reg/2009/78/2013-07-01, 2013.

[61] X. Lv, Z. Xiao, J. Fang, Q. Li, F. Lei, G. Sun, On safety design of vehicle for protection of vulnerable road users: a review, Thin-Walled Struct. 182 (2023) 109990, https://doi.org/10.1016/j.tws.2022.109990.

[62] Afdhal, O. Jirousek, P.S. Palar, J. Falta, Y.B. Dwianto, Design exploration of additively manufactured chiral auxetic structure using explainable machine learning, Mater. Des. 232 (2023) 112128, https://doi.org/10.1016/j.matdes.2023.112128.